Supporting Information

Donor–acceptor iron phthalocyanine-based hyper-crosslinked polymers with modulated electronic structure for efficient oxygen reduction reaction in aluminum-air batteries

Xinran Dong[a,1], Yingjian Luo[a,1], Shuhui Tao[b], Jiayao Liu[a], Xing Tan[a], Ze Lu[a], Gang Wang[a], Jinwei Chen[a], Ruilin Wang[a,*], and Jie Zhang[a,*]

[a]College of Materials Science and Engineering, Sichuan University, Chengdu, 610065, China

[b]National University of Singapore (Chongqing) Research Institute, Chongqing, 401123, China

[1]Xinran Dong and Yingjian Luo contributed equally to this work.

*Corresponding authors at: College of Materials Science and Engineering, Sichuan University, No.24 South Section 1, Yihuan Road, Chengdu 610065, P.R. China. Tel: +86-028-85418786;

E-mails address: rl.wang@scu.edu.cn (Ruilin Wang), jzhangchem@scu.edu.cn (Jie Zhang)

Physical characterization

The structure and morphological information of catalysts were obtained by X-ray diffraction patterns (XRD) on DX-2700B (HAOYUAN Instrument, China) equipped with CuKα radiation (λ=1.54 Å). Scanning electron microscopy (SEM) was carried out with SIGMA500 (Zeiss, Germany). The transmission electron microscopy (TEM) and aberration-corrected High Angle Angular Dark Field-Scanning Transmission Electron Microscopy (HAADF-STEM) measurements were taken on the FEI-Talos F200S/FEI Tecnai F20 X-Twin instrument. The specific surface areas were calculated by using the Brunauer-Emmett-Teller (BET) method and the pore size distributions were determined by the Barrett–Joyner–Halenda (BJH) method on Quantachrome system (NOVA2200e) via nitrogen adsorption/desorption measurement. Chemical compositions and surface states of catalysts were examined by X-ray photoelectron spectroscopy (XPS) on Escalab Xi+ (Thermo Fisher Co.). Raman spectra were recorded with Dxr2xi spectrometer using the excitation wavelength of 532 nm. Fourier transform infrared (FTIR) spectra were collected on a Bruker ALPHA II spectrometer. Thermogravimetric analysis-differential thermal analysis (TGA-DTA) curves were collected on NETZSCH (STA449 F3) with the heating rate of 5 ℃ min^{-1} under Ar flow. Absorption spectra were measured on UV-vis spectrophotometer (UV-3600i Plus, Shimadzu Co.). Atomic force microscopy (AFM) images were recorded on a DimensionXR (BRUKER). Solid-state ^{13}C NMR spectra (ssNMR) were recorded on Agilent-NMR-VNMRS 600.

Electrochemical measurements

Metrohm Autolab workstation system equipped with rotating disk electrode (RDE, Pine Instruments Co. Ltd., USA) was used to perform the electrochemical characterizations. All the electrochemical measurements were performed in a typical three-electrode system. Graphite plate and Hg/HgO electrode were used as the counter electrode and reference electrode, respectively. To prepare the working electrode, 5 mg of as-prepared catalyst and 50 μL of 5 wt% Nafion were dispersed into a mixed solvent containing 0.5 mL ethanol and 0.5 mL deionized water. For ORR measurement, the mixed solution was sonicated for 30 min to form a homogeneous catalyst ink, of which 10 μL of ink was dropped on the glass carbon (GC) electrode (0.196 cm^2) to obtain a loading of ~255 μg_{cata} cm^{-2}. Commercial Pt/C catalyst ink was also loaded on GC for comparison. Prior to each ORR measurement, the electrolyte solution was purged with Ar and/or O_2. The working electrode was activated by performing 30 cycles of cyclic voltammetry (CV) scans at a scan rate of 100 mV s^{-1}, ensuring that stable current could be obtained in the subsequent measurements. Linear sweep voltammetry (LSV) curves were recorded in O_2-saturated 0.1 M KOH at 400 to 2025 rpm with 10 mV s^{-1} using RDE. The electron transfer number (n) during the ORR is calculated according to Koutecky–Levich (K–L) equation:

$$\frac{1}{J}=\frac{1}{J_K}+\frac{1}{J_L}=\frac{1}{J_K}+\frac{1}{B\omega^{1/2}}$$

$$B=0.2nF(D_o)^{2/3}\nu^{-1/6}C_o$$

where J is the measured current density, J_L and J_k are the limiting diffusion- and kinetic current density, ω is the electrode rotation rate, n is the transferred electron number. F

is the Faraday constant (96485 C mol^{-1}), C_O is the O_2 concentration in electrolyte (1.2×10^{-6} mol cm^{-3}), D_O is the diffusion coefficient of O_2 (1.9×10^{-5} cm^2 s^{-1}), and v is the kinetic viscosity (0.01 cm^2 s^{-1}).

ECSA values were estimated via the formula ($ECSA=C_{dl}/C_s$), where C_{dl} is the double layer capacitance obtained from the slope of the linear fitting of capacitive currents vs. scan rates. C_s is the specific capacitance of the sample (adopted as 0.04 mF cm^{-2} here) or the capacitance of an atomically smooth planar surface of the material per unit area under identical electrolyte condition. CV measurements were conducted at scan rates ranging from 20 to 100 mV s^{-1}. The measured current in the CV curves was caused by the double-layer charging (I_c). The C_{dl} was calculated as the double-layer charging current divided by the scan rate (v): $C_{dl} = I_c/v$. The linear response of a charge difference to a voltage difference of a capacitor $\Delta Q=C\ \Delta U$, the derivative in time equals $I = C\ v$.

All the potentials in this work were converted to a reversible hydrogen electrode (RHE) using the following equation: $E(RHE)=E(Hg/HgO) + \varphi(Hg/HgO) + 0.059\times pH$. Electrochemical impedance spectroscopy (EIS) was conducted at 0.9 V in the 100 kHz to 0.1 Hz ranges using a 5 mV of amplitude sinusoidal signal.

Assembly and measurements of liquid Al-air battery

For the fabrication and measurement of battery, the polished aluminum plates (thickness: 3 mm) was served as the anode. 6 M KOH solution containing 0.01 M Na_2SnO_3, 0.0005 M $In(OH)_3$, and 0.0075 M ZnO were used as the electrolyte. The air electrode was prepared by mixing catalyst with deionized water, isopropanol, and

Nafion (volume ratio of 10:10:1) to form the homogeneous catalyst slurry. The obtained catalyst slurry was dropwise dropped onto the gas diffusion layer (GDL, composing of hydrophobic carbon paper and nickel foam), followed by dried at 70 ℃ to achieve the loading of 1 mg_{cata} cm^{-2}. For comparison, Pt/C was also dropped onto the GDL with the same loading. The polarization curves were obtained at the scan rate of 20 mV s^{-1} on electrochemical workstation system. Galvanostatic charge/discharge performance was executed on LAND CT2001A instrument.

Assembly of flexible Al-air battery

The flexible Al-air batteries were tested in laboratory-constructed electrochemical cells. For synthesizing poly (acrylic acid) (PAA) gel electrolyte, 18 g KOH and 0.6 g ZnO were dissolved into 26 mL of deionized water, named as solution A. 3 g acrylic acid were adequately mixed with 0.5 g N,N"-methylenebis-acrylamide, named as solution B. After that, solution B was added into solution A, and then vigorously stirred for 10 min. After removing the white sediment, the polymer solution was transferred into the mold, and 50 μL of saturated $K_2S_2O_8$ solution was dropped into the polymer solution as initiator with vigorously stirring until the PAA gel formed.

For the fabrication of flexible all-solid-state Al-air battery, Al foils (thickness: 0.2 mm) was served as the anode. The air electrode was prepared by mixing catalyst, acetylene black, and polytetrafluoroethylene with mass ratio of 8:1:1 in mixed solution of ethanol and Nafion. The obtained slurry was dropwise dropped on the carbon cloth (CC), followed by dried at 70 ℃ to achieve the loading of 1 mg_{cata} cm^{-2}. For comparison, the mixture of Pt/C were also dropped onto the CC with the same loading.

The aluminum foil coated with PAA and the air electrode were stacked together, and the assembled flexible all-solid-state Al-air battery was sealed with porous bandage.

Computational methods

We have employed the Vienna Ab-initio Simulation Package (VASP) to perform all Spin-polarization density functional theory (DFT) calculations within the generalized gradient approximation (GGA) using the Perdew-Burke-Ernzerhof (PBE) formulation. We have chosen the projected augmented wave (PAW) potentials to describe the ionic cores and take valence electrons into account using a plane wave basis set with a kinetic energy cut off of 400 eV. The Brillouin zone integration is performed using 1×1×l Monkhorst-Pack k-point sampling for surface and interface due to a large number of atoms (Fe atoms: 1, S atom: 8, N atom: 8, C atom: 36)[3]. The electronic energy was considered self-consistent when the energy change was smaller than 10^{-5} eV. A geometry optimization was considered convergent when the energy change was smaller than 0.03 eV $Å^{-1}$. The Gibbs reaction free energy change (ΔG) of each elementary step in the ORR was evaluated based on the computational hydrogen electrode (CHE) model developed by Nørskov and coworkers. The four-electron ORR mechanism in alkaline medium can be summarized as follows:

$$O_2(g) + H_2O(l) + e^- + * \leftrightarrow *OOH + OH^-$$

$$*OOH + e^- \leftrightarrow *O + OH^-$$

$$*O + H_2O(l) + e^- \leftrightarrow *OH + OH^-$$

$$*OH + e- \leftrightarrow * + OH^-$$

$$\text{Overall: } O_2(g) + 2H_2O + 4e^- \leftrightarrow 4OH^-$$

where * represents an active site. (l) and (g) refer to liquid and gas phases, respectively, and O*, OH* and OOH* are adsorbed intermediates.

The free energy (ΔG) is obtained by $\Delta G = E_{DFT} + \Delta ZPE - T\Delta S + \Delta G_U$, where E_{DFT} is the energy difference of reactants and products. obtained from DFT calculations; ΔZPE and ΔS are the contributions to the free energy from the zero-point vibration energy and entropy, respectively. T is the temperature (298.15 K). $\Delta G_U = -eU$, here U is the potential at the electrode and e is the transferred charge.

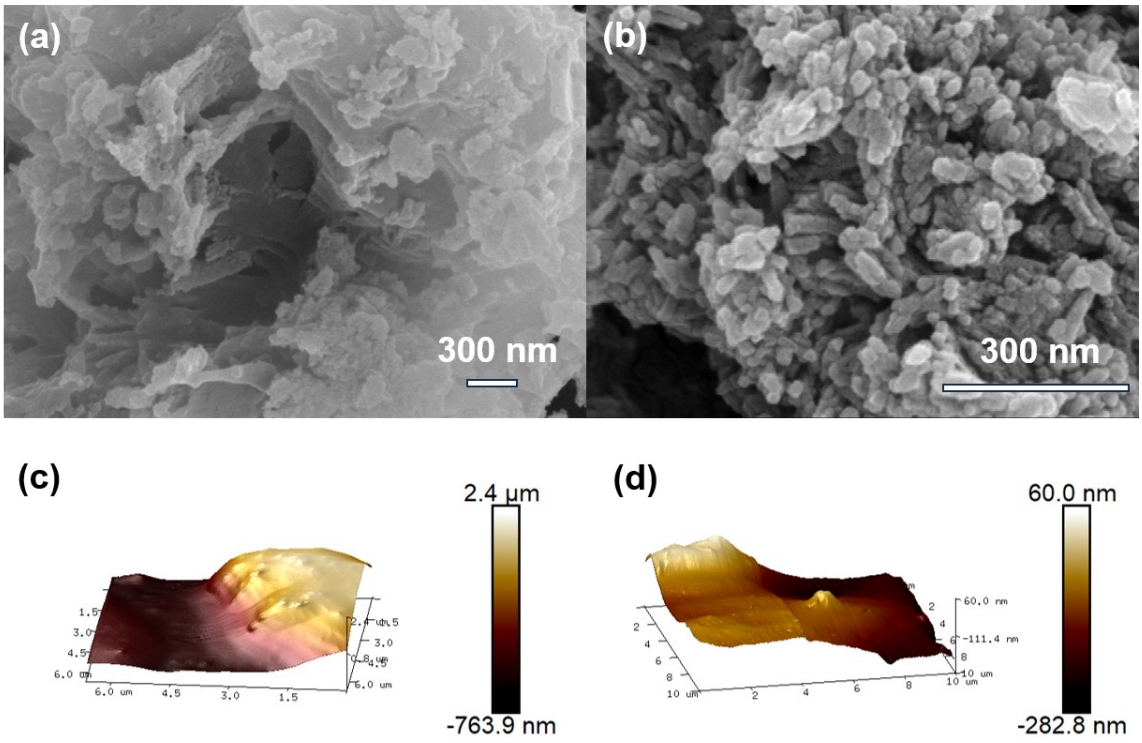

Figure S1 SEM images and AFM topographical maps of (a, c) pFePc-TTF and (b, d) commercial FePc after ultrasonic exfoliation.

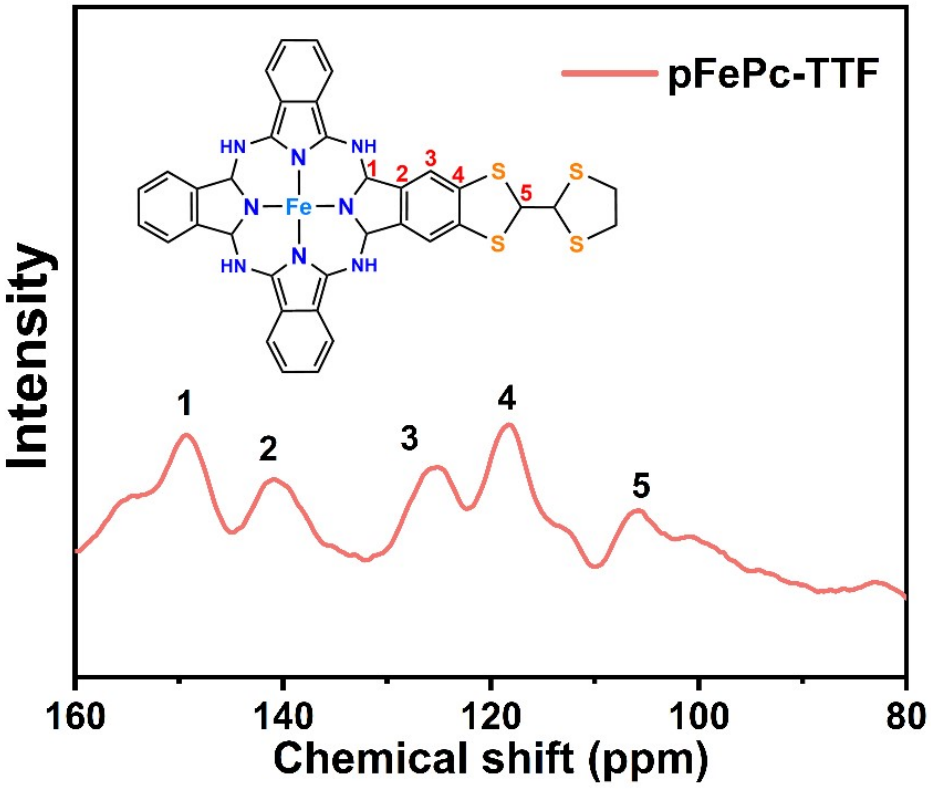

Figure S2 Solid-state ^{13}C-NMR spectrum of pFePc-TTF.

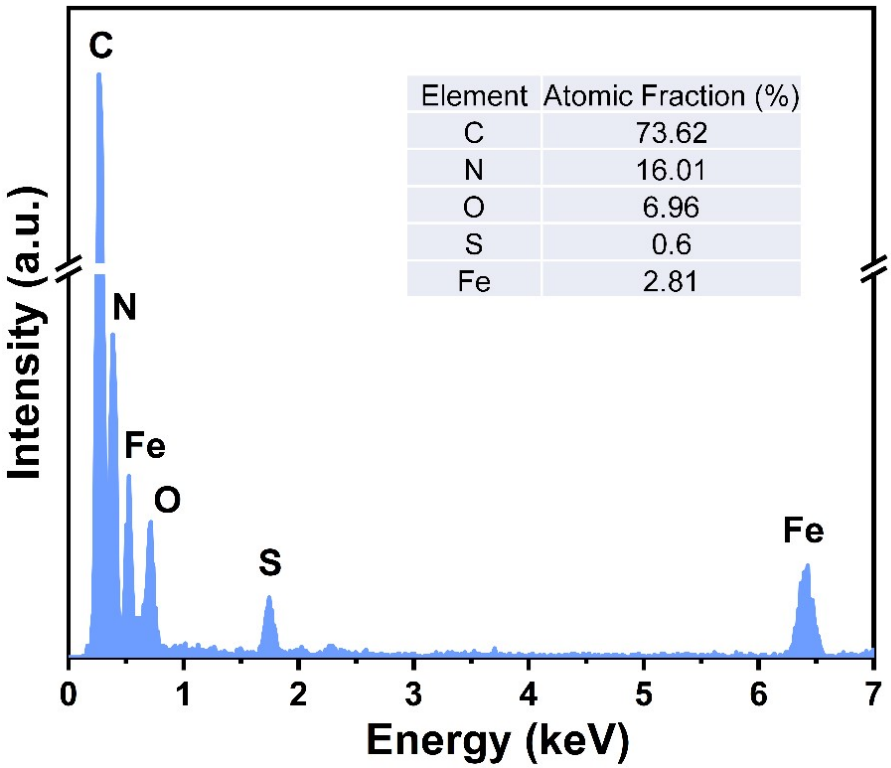

Element	Atomic Fraction (%)
C	73.62
N	16.01
O	6.96
S	0.6
Fe	2.81

Figure S3 EDX spectrum of pFePc-TTF.

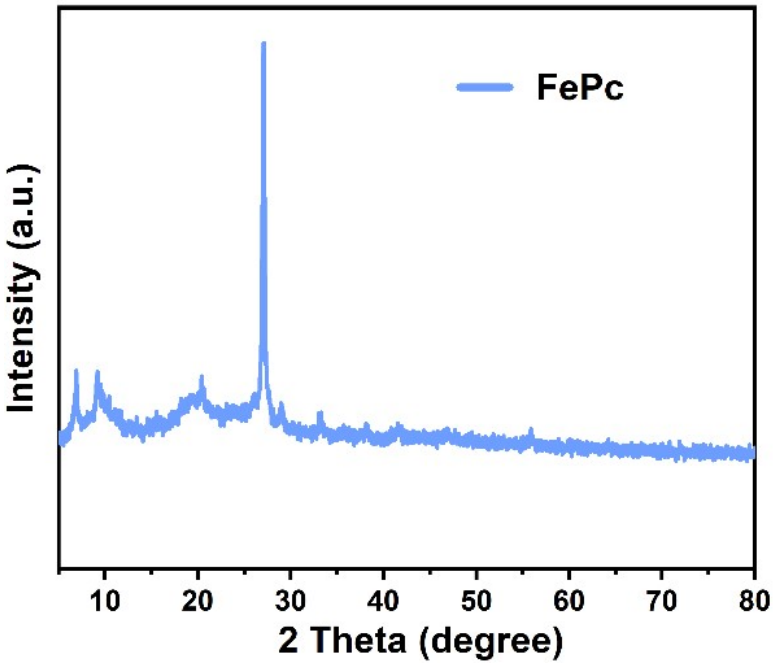

Figure S4 XRD pattern of FePc monomer.

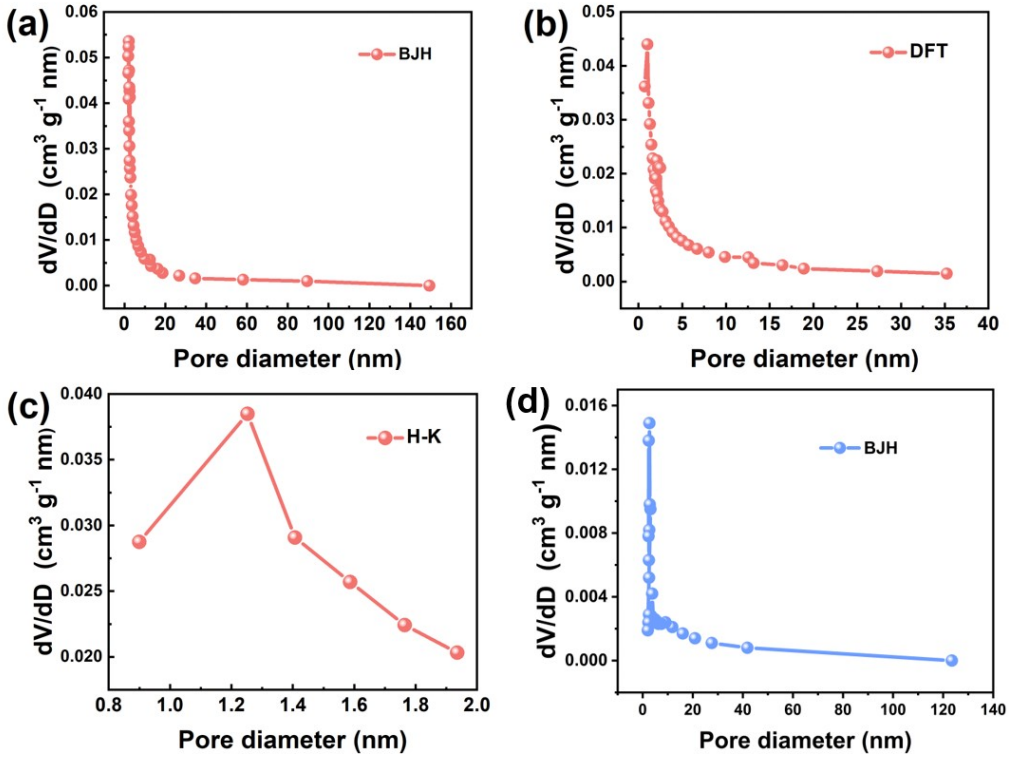

Figure S5 Pore distributions of the pFePc-TTF analyzed by (a) BJH method, (b) DFT method, (c) H-K method, respectively. (d) Pore distribution of the FePc analyzed by BJH method.

Table S1. Properties of pore structures on the pFePc-TTF and FePc.

Catalysts	S_{BET} (m^2 g^{-1})[a]	S_{micro} (m^2 g^{-1})[b]	Pore size distribution (nm)[c]	Pore size distribution (nm)[d]	V_t (cm^3 g^{-1})[e]	V_{micro} (cm^3 g^{-1})[f]
pFePc-TTF	151.95	39.70	1.02	3.46	0.37	0.33
FePc	13.87	0	-	2.42	0.08	-

a. S_{BET} is the Brunauer-Emmett-Teller (BET) specific surface area.

b. S_{micro} is calculated from nitrogen adsorption-desorption isotherm by T-plot method.

c. Pore size distribution is obtained by using DFT method.

d. Pore size distribution is obtained by using BJH method.

e. V_t is the total specific pore volume determining by using the absorption branch at P/P_0=0.99.

f. V_{micro} is micropore volume calculated from nitrogen adsorption-desorption isotherm by using DFT method.

Table S2 The contents of different N species obtained from high resolution N 1s spectra of pFePc-TTF and pFePc.

Catalysts	Pyrrole-N (%)	Fe-N (%)	Pyridinic-N (%)
pFePc-TTF	16.08	53.17	31.75
pFePc	30.64	38.30	31.06

Note: The content percentage of a certain N specie is equal to the total area of all these three N species divided by its corresponding area, which obtains from the integral area of peak.

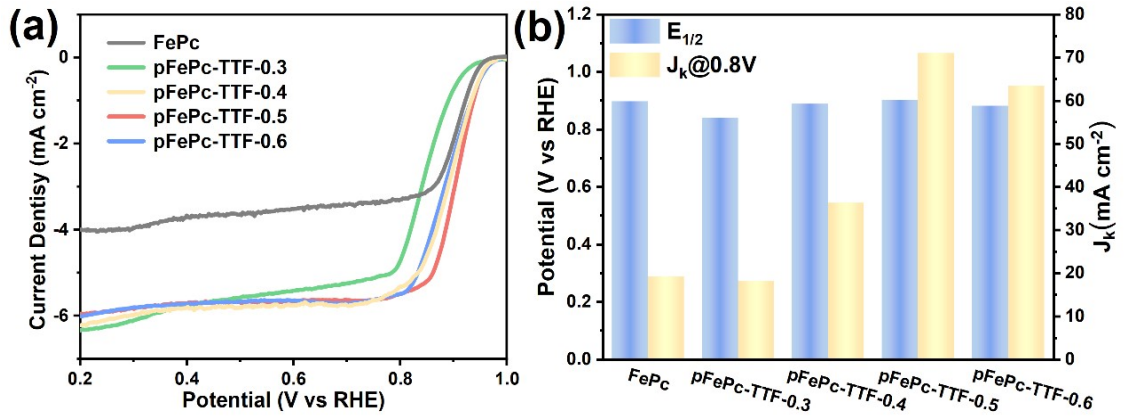

Figure S6 (a) LSV curves and (b) Comparison of $E_{1/2}$ and J_k@0.8 V obtained from pFePc-TTF-*x* catalysts with different contents of TTF (*x* represent the molar ratio of TTF and FePc, in which the content of FePc was fixed at 0.4 mmol).

Table S3 Comparison of pFePc-TTF and other reported catalysts for ORR in 0.1 M KOH electrolyte.

Catalysts	**E_{onset}** (V)	**$E_{1/2}$** (V)	**J_L** (mA cm^{-2})	**Catalyst loading** (μg cm^{-2})	**Ref.**
pFePc-TTF	0.98	0.90	5.95	255	**This work**
DMC–FePc-15	0.92	0.86	5.4	383	[1]
FeN_4S_1	0.96	0.88	5.71	255	[2]
Fe-N_4/NP-PHC	1.0	0.89	5.75	—	[3]
Fe,P,N-Carbon	0.97	0.89	5.75	—	[4]
Fe_2P/NPCs	0.95	0.82	5.58	509	[5]
Fe-N/P-C-700	0.94	0.867	5.66	600	[6]
SA&NP-FeCo-NTS	0.98	0.87	5.7	600	[7]
Fe/N-MGN	0.97	0.882	5.87	204	[8]

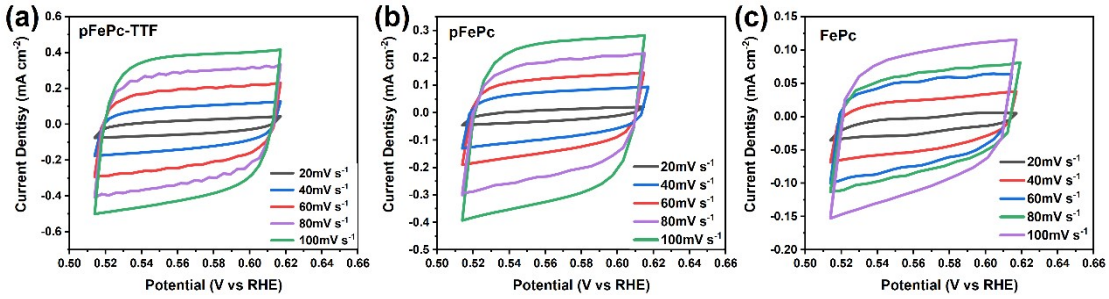

Figure S7 CV curves of (a) pFePc-TTF, (b) pFePc, and (c) FePc at different scan rates in 0.1 M KOH.

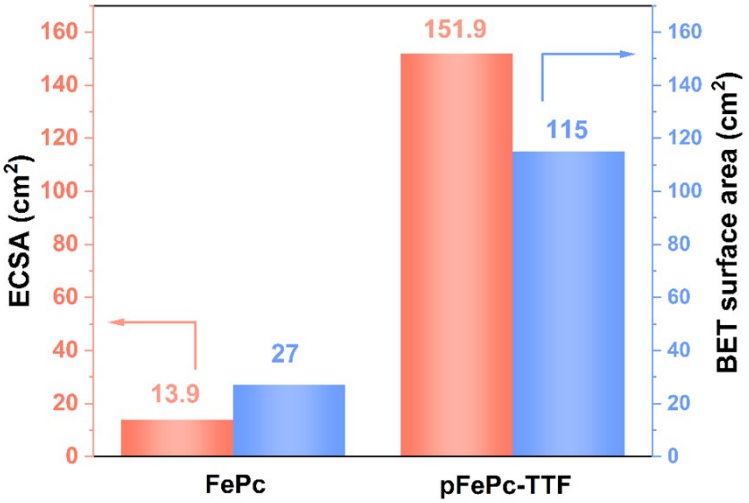

Figure S8 Comparison of the ECSA and BET surface area of pFePc-TTF and FePc.

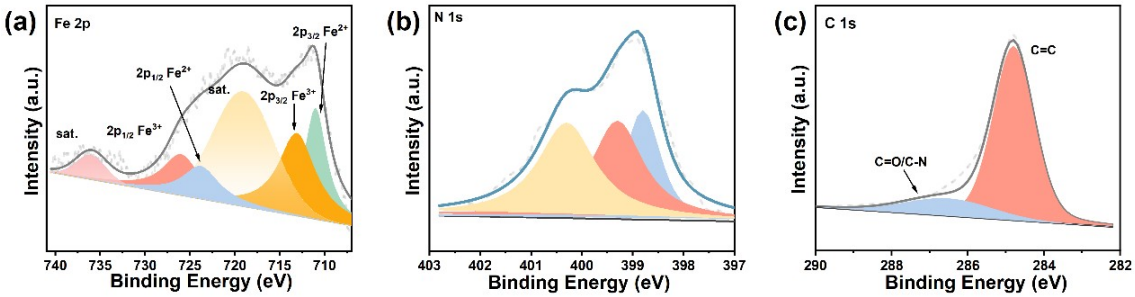

Figure S9 High-resolution XPS spectra of (a) Fe 2p, (b) N 1s, and (c) C 1s for pFePc-TTF after ADT.

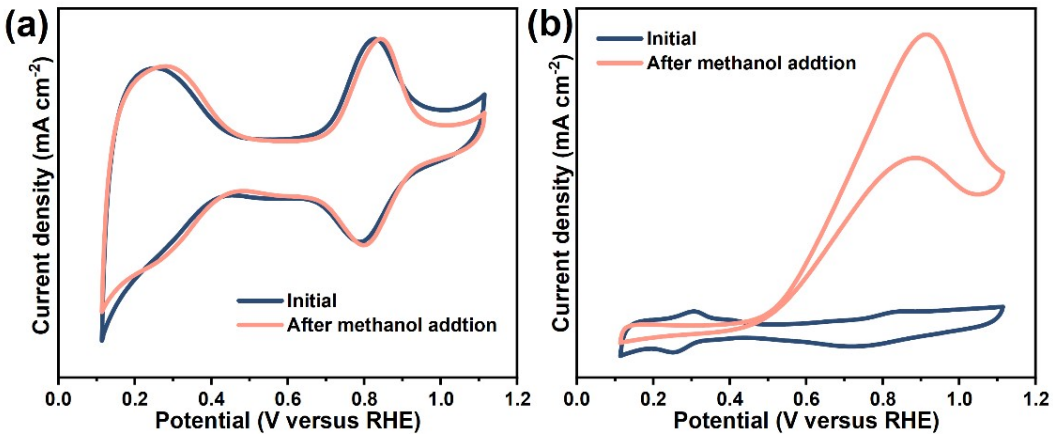

Figure S10 CV curves of initial catalysts and after adding 3 M methanol in 0.1 M KOH: (a) pFePc-TTF and (b) Pt/C.

Table S4 Comparison of pFePc-TTF catalyst and other reported catalysts for Al-air batteries.

Catalysts	OCV (V)	P_{max} (mW cm^{-2})	Ref
pFePc-TTF	1.93	218.34	**This work**
Ag-Cu25/NPC	1.89	193	[9]
Fe/Ce-NCNT-0.2	1.81	164	[10]
CoNi@NCNTs/CC	1.68	221	[11]
FePc@HNSC	1.92	204.9	[12]
Fe-BCN	1.83	195.2	[13]
SA-Fe-N_x-MPCS	1.53	130	[14]
PNC-B	1.40	75.4	[15]
0.8-CoNCNTs/CP	1.79	159.6	[16]

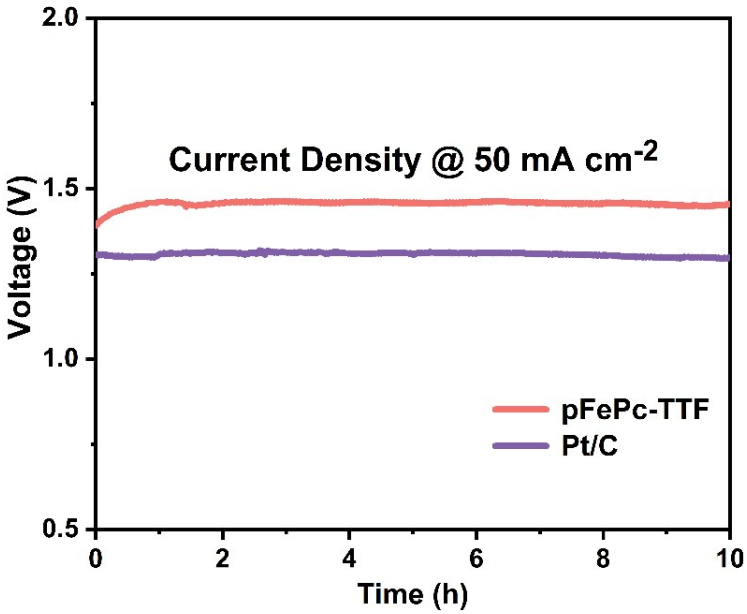

Figure S11 Discharge curves of AAB with pFePc-TTF and Pt/C as air cathodes at 50 mA cm^{-2}.

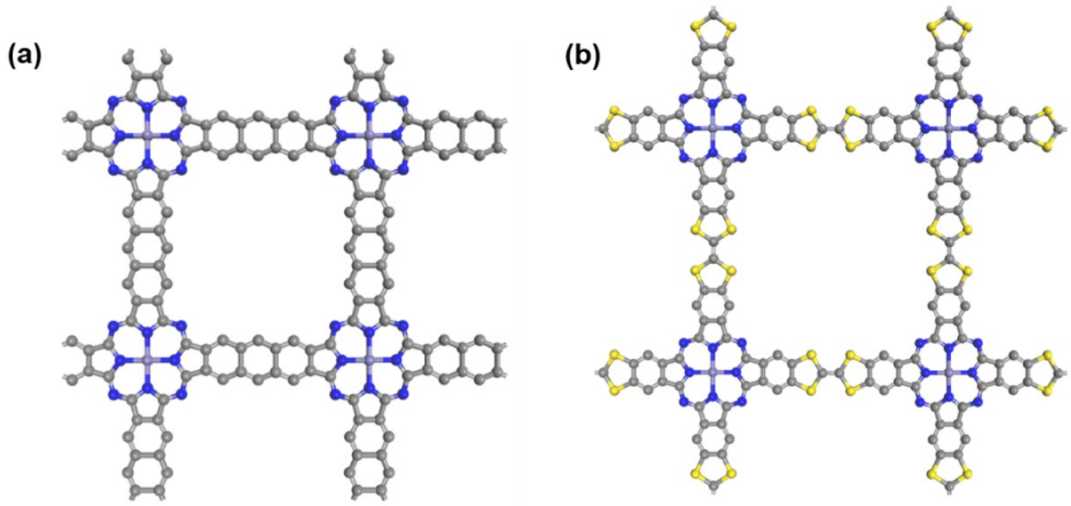

Figure S12 DFT models of (a) pFePc and (b) pFePc-TTF.

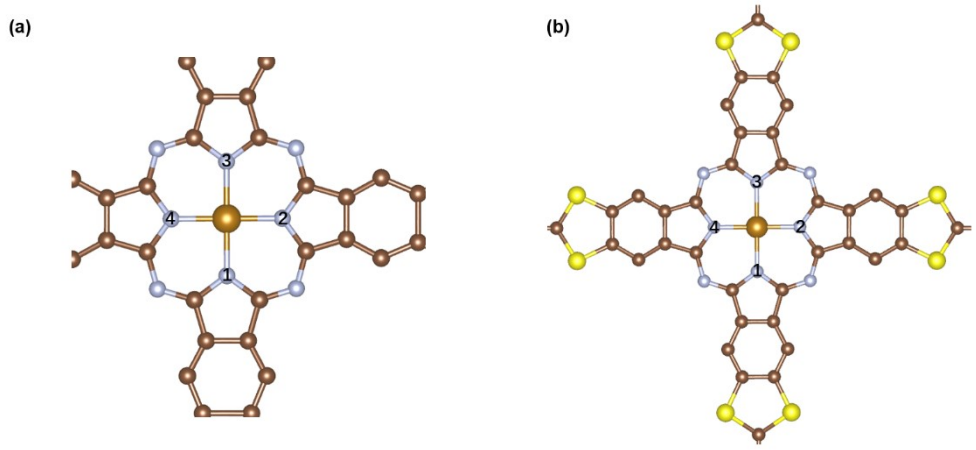

Figure S13 Bader charge of N and Fe atoms in (a) pFePc and (b) pFePc-TTF.

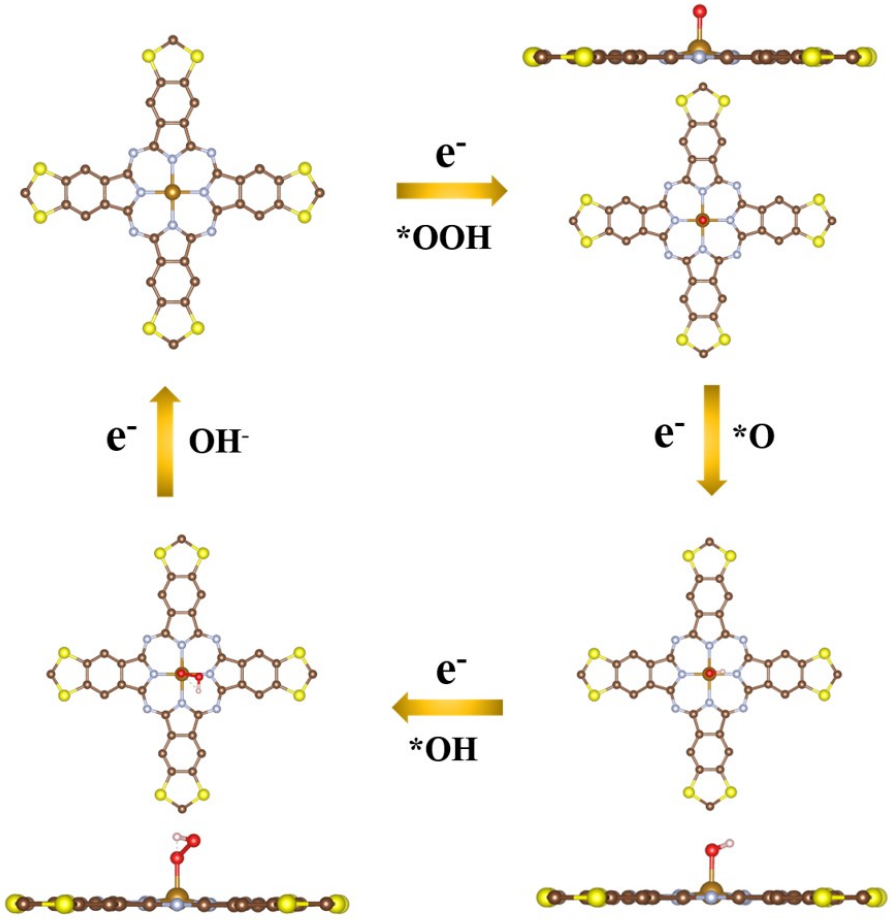

Figure S14 Atomic configurations of oxygen intermediates adsorbed on Fe-N_4 sites of pFePc-TTF (yellow atoms for sulfur, brown atoms for carbon, gray atoms for nitrogen, red atoms for oxygen, and write atoms for hydrogen).

Reference

[1] M. Wang, Y. Wu, X. Li, Y. Wang, X. Wu, G. Li, L. Yang, Y. Lin, Nanoscale 23 (2022) 8255-8259.

[2] Y. Zhang, C. Li, J. Li, X. Liu, G. Li, B. Li, L. Wang, J. Mater. Chem. A 11 (2023) 11326-11333.

[3] J. Li, K.C. Fan, H.L. Jiang, F.H. Lu, L.X. Cui, B. Li, Q. Zhang, G.C. Fan, L.B. Zong, L. Wang, J. Mater. Chem. A 35 (2022) 18147-18155.

[4] Y.A. Li, Z.L. Xu, X.H. Sun, J. Han, R. Guo, J. Colloid Interface Sci. 602 (2021) 376-383.

[5] R.X. Wang, Y.L. Yuan, J.B. Zhang, X.C. Zhong, J.M. Liu, Y.M. Xie, S.P. Zhong, Z.F. Xu, J. Power Sources 501 (2021) 10.

[6] K. Yuan, D. Lutzenkirchen-Hecht, L.B. Li, L. Shuai, Y.Z. Li, R. Cao, M. Qiu, X.D. Zhuang, M.K.H. Leung, Y.W. Chen, U. Scherf, J. Am. Chem. Soc. 5 (2020) 2404-2412.

[7] Q. Zhang, P.F. Liu, X.G. Fu, Y. Yuan, L.G. Wang, R. Gao, L.R. Zheng, L. Yang, Z.Y. Bai, Adv. Functional Mater. 22 (2022) 9.

[8] L.B. Li, S.H. Huang, R. Cao, K. Yuan, C.B. Lu, B.Y. Huang, X.N. Tang, T. Hu, X.D. Zhuang, Y.W. Chen, Small 2 (2022) 12.

[9] J. Wang, A. Wu, L. Xing, S. Ran, W. Yu, X. Dong, H. Huang, J. Energy Chem. 86 (2023) 217-226.

[10] J. Wang, A. Wu, Z. Qiu, A. Li, W. Qin, H. Huang, Appl. Surf. Sci. 608 (2023) 155185.

[11] W. W. Tian, J. T. Ren, Z. Y. Yuan, Appl. Catal. B: Environ. 317 (2022) 121764.

[12] Y. Luo, Y. Chen, Y. Xue, J. Chen, G. Wang, R. Wang, M. Yu, J. Zhang, Small 2 (2022) 2105594.

[13] X. Kang, G. Fu, F. Si, X. Deng, L. Wang, X. Z. Fu, J. L. Luo, Int. J. Hydrogen Energy 73 (2021) 36221-36231.

[14] X. Fu, G. Jiang, G. Wen, R. Gao, S. Li, M. Li, J. Zhu, Y. Zheng, Z. Li, Y. Hu, L. Yang, Z. Bai, A. Yu, Z. Chen, Appl. Catal. B: Environ. 293 (2021) 120176.

[15] H. Yu, H. Zhang, Z. Zhang, ChemCatChem 1 (2021) 397-406.

[16] S. Liu, Z. Cao, Y. Meng, Y. Li, W. Yang, Z. Chang, W. Liu, X. Sun, ACS Appl. Mater. Interfaces 23 (2021) 26853-26860.